Nano Research 2016, 9(8): 2498–2509
DOI 10.1007/s12274-016-1136-4
Research Article
ISSN 1998-0124
CN 11-5974/O4

N-doped graphene grown on silk cocoon-derived interconnected carbon fibers for oxygen reduction reaction and photocatalytic hydrogen production

Yongpeng Lei[1] (✉), Qi Shi[2,4], Cheng Han[2], Bing Wang[2], Nan Wu[2], Hong Wang[2], and Yingde Wang[2,3] (✉)

[1] *College of Basic Education, National University of Defense Technology, Changsha 410073, China*
[2] *Science and Technology on Advanced Ceramic Fiber and Composites Laboratory, National University of Defense Technology, Changsha 410073, China*
[3] *College of Materials Science and Engineering, Wuhan Textile University, Wuhan 430074, China*
[4] *Luoyang Ship Material Research Institute, Luoyang 471039, China*

Received: 7 February 2016
Revised: 5 May 2016
Accepted: 8 May 2016

KEYWORDS
N-doped graphene,
silk cocoon,
interconnected carbon fibers,
oxygen reduction reaction,
photocatalytic hydrogen production

ABSTRACT

Carbon-based metal-free catalysts are a promising substitute for the rare and expensive platinum (Pt) used in the oxygen reduction reaction. We herein report N-doped graphene (NG) that is exquisitely integrated into highly conductive frameworks, simultaneously providing more active sites and higher conductivity. The NG was *in situ* grown on carbon fibers derived from silk cocoon (SCC_f) using a simple one-step thermal treatment. The resulting product (NG-SCC_f), possessing a meso-/macroporous structure with three-dimensional (3D) interconnected networks, exhibits an onset potential that is only 0.1 V less negative than that of Pt/C and shows stability and methanol tolerance superior to those of Pt/C in alkaline media. Moreover, in the absence of Pt as co-catalyst, NG-SCC_f shows a photocatalytic H_2 production rate of 66.0 $\mu mol \cdot h^{-1} \cdot g^{-1}$, 4.4-fold higher than that of SCC_f. This outstanding activity is intimately related to the *in situ* grown NG, hierarchically porous structure, and 3D interconnected networks, which not only introduce more active sites but also enable smooth electron transfer, mass transport, and effective separation of electron-hole pairs. Considering the abundance of the green raw material in combination with easy and low-cost preparation, this work contributes to the development of advanced sustainable catalysts in energy storage/conversion fields, such as electro- and photocatalysis.

1 Introduction

In view of the accelerated depletion of fossil fuels and the increasing global energy crisis, fuel cells (FCs) have emerged as the ideal power source for non-polluting vehicles. The design of highly active, stable,

Address correspondence to Yongpeng Lei, lypkd@163.com; Yingde Wang, wangyingde@nudt.edu.cn, wyd502@163.com

and cheap electrocatalysts to replace Pt/C [1–4] in the oxygen reduction reaction (ORR) at the cathode has aroused great attention for direct methanol FCs [5, 6]. Being the most promising alternative, carbon-based metal-free catalysts not only possess the advantages of low cost, abundance, and easy accessibility, but also have an easily tailored composition and a tunable pore structure [7–13]. To improve electrocatalytic activity, heteroatoms like N, B, P, O, and S are often used to dope carbon materials, facilitating the chemical adsorption of oxygen and providing more effective active sites [14–16]. However, the incorporated heteroatoms may decrease conductivity and thus hinder charge transport to some extent [17, 18].

A promising solution is to integrate N-doped graphene (NG) into highly conductive frameworks, which simultaneously provides more active sites and higher conductivity [19]. Recently, Qiao's group [20] prepared N-doped ordered macro-/mesoporous carbon/graphene demonstrating superior electrocatalytic activity. Two templates (requiring further removal) with different diameters were used to generate macro- and mesopores simultaneously. Biomass, having advantages like extensive availability, environmental friendliness, and renewability, is an effective precursor to heteroatom-doped carbon materials for ORR and other applications [21–23]. By calcining a mixture of bacterial cellulose and urea, Chen et al. [24] prepared a "vein-leaf" type of three-dimensional (3D) carbon nanofibers with *in situ* grown NG. The onset potential of this material is ca. 0.1 V more negative than that of the commercial Pt/C catalyst. However, the time-consuming freeze-drying procedure employed to provide a high surface area results in low efficiency. Furthermore, N-doped high-surface-area carbon materials for electrocatalytic applications were also prepared by simple thermal treatment of biomass such as cotton [25], amaranthus [26], tea leaves [27], hair [28], etc., greatly emphasizing the untapped potential of biomass and simplifying the preparation processes.

Electrospinning is a versatile method for producing 3D continuous nanofibers on a large scale, with great potential for energy applications, such as supercapacitors, FCs, metal-air batteries, etc. [29–31]. Silk cocoon, produced by an electrospinning-like process, is an example of abundantly available natural biomass with a largely unexplored potential use in energy storage and transformation. Lately, Wu and coworkers [32] prepared binder-free supercapacitor electrodes by direct carbonization of silk cocoon, utilizing the interconnected 3D porous network structure and flexibility of carbonized silk cocoon (SCC_f). In our previous work, cross-linked Fe-N/C nanofiber networks [33] and cobalt-containing carbon nanofibers interconnected by *in situ* grown NG/carbon nanotubes (CNTs) [34, 35] were prepared by electrospinning and subsequent thermal treatment. These non-precious metal 3D networks show excellent ORR activity due to efficient electron transfer, mass transport, and highly abundant active sites.

In this study, NG was *in situ* grown on SCC_f using a one-pot thermal treatment of graphitic carbon nitride ($g\text{-}C_3N_4$), melamine, and silk cocoon, which not only introduces more active sites but also accelerates the mass and electron transport for oxygen reduction. The product ($NG\text{-}SCC_f$) shows superior ORR catalytic behavior (with the onset potential being only 0.1 V more negative than that of the Pt/C catalyst), close to four-electron ($4e^-$) transfer processes, and good methanol tolerance in alkaline media. It is worth mentioning that the metal-free $NG\text{-}SCC_f$ shows an H_2 production rate of 66.0 $\mu mol \cdot h^{-1} \cdot g^{-1}$ in absence of a co-catalyst, which is 4.4-fold higher than that of SCC_f. This behavior can be attributed to rapid charge transfer and effective separation of electron–hole pairs. Furthermore, the easy low-cost method facilitates large-scale production. We hope that this work will provide an innovative strategy for preparing metal-free catalysts with well-tailored architecture and composition for applications in energy- and environment-related fields.

2 Experimental

Bombyx mori silk cocoon was purchased from Taobao. Melamine was purchased from Tianjin Guangfu Fine Chemical Research Institute (China). $g\text{-}C_3N_4$ was prepared by heating melamine at 550 °C in air for 4 h. Isopropyl alcohol was purchased from Tianjin Damao Chemical Reagent Factory (China). Nafion solution (5 wt.%) and the Pt/C electrocatalyst (20 wt.% Pt) were purchased from Alfa Aesar and Johnson Matthey,

respectively. Ultrapure water was produced in-house. All reagents were used as received.

The preparation of NG-SCC_f, N-doped SCC_f (N-SCC_f), and SCC_f is illustrated in Scheme 1. SCC_f was obtained by heating silk cocoon at 900 ℃ (heating rate of 3 ℃·min^{-1}, final temperature maintained for 2 h). NG-SCC_f was prepared as follows. Untreated silk cocoon (0.2 g) was ground with melamine (1 g) and g-C_3N_4 (1 g). The mixture was transferred into a furnace under a flow of N_2 and further heated at 600 ℃ (1 ℃·min^{-1}) with a holding time of 1 h. Subsequently, the sample was heated to 900 ℃ (3 ℃·min^{-1}) with a holding time of 1 h and then cooled to room temperature under nitrogen to yield black NG-SCC_f. N-SCC_f (without *in situ* formed graphene) was obtained by heating SCC_f ground with g-C_3N_4 and melamine under the same conditions. Graphene oxide (GO) was prepared using an improved Hummer's method [36]. GO (0.3 g) and melamine (1.5 g) were dispersed in ultrapure water and stirred thoroughly. The mixture was heated at 120 ℃ for 7 h and subsequently at 900 ℃ for 1 h (3 ℃·min^{-1}) to obtain NG. In addition, the physical mixture of NG and N-SCC_f, referred to as MIX, was used as a control sample.

Sample morphology was characterized by field emission scanning electron microscopy (FESEM, Hitachi S-4800, Japan). Transmission electron microscopy (TEM) was performed using the TecnaiTF200 instrument. X-ray photoelectron spectroscopy (XPS) was carried out using a VG ESCALAB MKΠ instrument (Al Kα excitation, UK). X-ray diffraction (XRD) patterns were recorded on a powder X-ray diffractometer (Siemens D-5005, Cu-Kα radiation, Germany). Raman spectra were obtained using a 488 nm air-cooled Ar^+ laser with 1.3 mV intensity and a 50× objective (LabRAM HR, Horiba Jobin Yvon, France). Thermogravimetric analysis (TGA) was performed on a SDT Q600 instrument in N_2 (10 ℃·min^{-1}). Nitrogen adsorption data were recorded with a Micromeritics ASAP 2020 nitrogen adsorption apparatus (USA). The specific surface areas (S_{BET}) were calculated based on the nitrogen adsorption data using the Brunauer–Emmett–Teller (BET) method. Pore size distributions were evaluated using the Barrett–Joyner–Halenda (BJH) method.

Electrochemical measurements were performed using a computer-controlled potentiostat (CHI 660e, Chenhua, China) with a three-electrode electrochemical cell. The glassy carbon electrode (GCE, 7.065 mm^2) and rotating disk electrode (RDE-3A, ALS, Japan, 12.56 mm^2) loaded with catalyst served as the working electrode. Pt wire and a saturated calomel reference electrode (SCE) were used as the counter and reference electrode, respectively. All experiments were performed at room temperature. The catalysts were loaded onto GCE or RDE using the following procedure. All catalysts were dispersed in a mixture of water, isopropanol, and Nafion by sonication to obtain a concentration of 5 g·L^{-1}. Subsequently, 6 and 8 μL of these suspensions were transferred onto the polished GCE and RDE, respectively. Cyclic voltammetry (CV) curves were recorded at a scan rate of 100 mV·s^{-1} in O_2-saturated 0.1 M KOH electrolyte. Linear sweep voltammetry (LSV) curves were obtained for different RDE rotation speeds (400, 600, 900, 1,200, and 1,600 rpm) at a scan rate of 10 mV·s^{-1}. Methanol was introduced into the KOH electrolyte to determine the crossover resistance. Durability tests of NG-SCC_f and Pt/C electrocatalysts were conducted by potential cycling in O_2-saturated 0.1 M KOH for up to 2,000 cycles. In all tests, O_2 was bubbled into the electrolyte to keep it saturated. The electron transfer numbers (n) of catalysts were obtained from the slopes of Koutecky–Levich (K–L) plots using the following equation (Eq. (1))

$$\frac{1}{j}=\frac{1}{j_k}+\frac{1}{B\omega^{0.5}} \quad (1)$$

where j is the disk current density, j_k is the kinetic current density, ω is the electrode rotation speed, and B is expressed as Eq. (2)

$$B=0.2nF(D_{O_2})^{2/3}\nu^{-1/6}C_{O_2} \quad (2)$$

where 0.2 is a conversion factor for expressing the rotation speed in rpm, F is the Faraday constant (F = 96,485 C·mol^{-1}), D_{O_2} is the diffusion coefficient of O_2 in 0.1 M KOH (1.9 × 10^{-5} cm^2·s^{-1}), v is the kinematic viscosity of the KOH solution (0.01 cm^2·s^{-1}), and C_{O_2} is the dissolved O_2 concentration (1.2 × 10^{-6} mol·cm^{-3}).

Photocatalytic H_2 production was carried out in a 100 mL three-neck quartz flask. A 300-W xenon arc

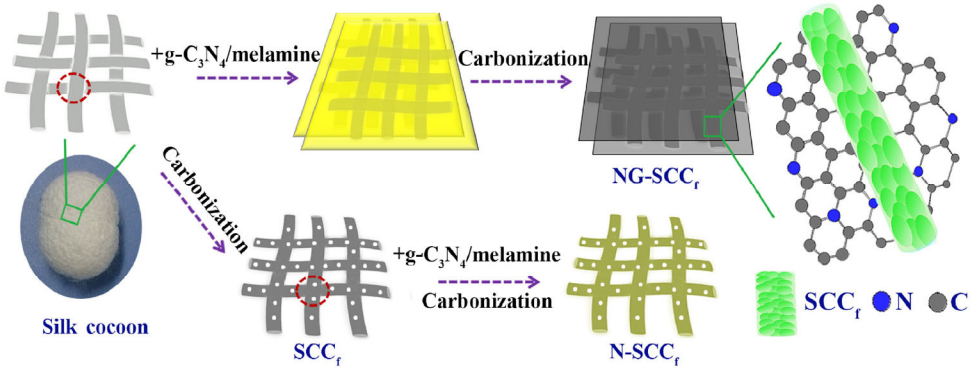

Scheme 1 Schematic diagram of the preparation of NG-SCC_f.

lamp (Changzhou Siyu Environmental Materials Co., Ltd.) positioned 20 cm away from the reactor was used as a solar light source to trigger the photocatalytic reaction. In a typical experiment, 20 mg of the prepared sample were dispersed in 50 mL of aqueous methanol (40 mL water and 10 mL methanol) under constant stirring. Prior to irradiation, the system was purged with nitrogen for 30 min to eliminate any residual O_2. After irradiation, the generated gas (1 mL) was intermittently collected and analyzed by gas chromatography (SP6890, Shangdong Lunan Ruihong Instrument Co., Ltd., TCD, argon carrier gas, and a 5 Å molecular sieve column).

3 Results and discussion

The preparation of NG-SCC_f, N-SCC_f, and SCC_f is illustrated in Scheme 1. The microstructure of these materials was analyzed by SEM and TEM (Fig. 1). The SEM image in Fig. 1(a) shows SCC_f with a diameter of ~10 μm. The inset indicates that the abundant mesopores are uniformly distributed on the SCC_f surface. Note that the red circles in Fig. 1(a) highlight the 3D interconnected web structure produced by thermal treatment, which facilitates fast electron and mass transport [37]. Heating the mixture of SCC_f, g-C_3N_4, and melamine produces the 3D interconnected SCC_f web only (Fig. 1(b)), while graphene growth on SCC_f was observed during the pyrolysis of silk cocoon, g-C_3N_4, and melamine (Fig. 1(c)). The identity of the *in situ* grown NG was further verified by TEM imaging (Fig. 1(d)).

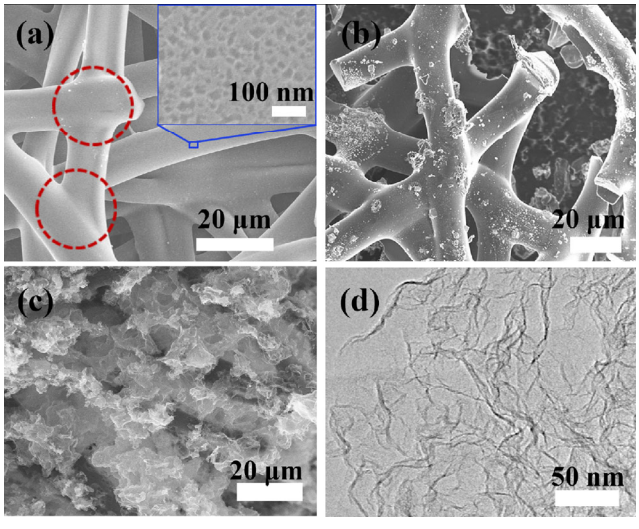

Figure 1 SEM images of (a) SCC_f, (b) N-SCC_f, (c) NG-SCC_f, and (d) TEM image of the *in situ* grown NG in NG-SCC_f.

XPS measurements were carried out to determine the content and the chemical states of N, C, and O (Fig. 2). Table 1 lists the chemical composition and the content of graphitic and pyridinic N for the three samples. The survey spectra (Fig. 2(a)) display three distinct peaks corresponding to the C, N, and O elements. The N content of SCC_f, N-SCC_f, and NG-SCC_f was determined to be 2.08 at.%, 3.71 at.%, and 7.19 at.%, respectively. The nitrogen in SCC_f originates from the amino acids (mainly glycine and alanine) in the cocoon, suggesting that it can act as a single precursor for both carbon and nitrogen. For NG-SCC_f and N-SCC_f, the increased N content is attributed to the complete decomposition of g-C_3N_4 and melamine N dopants at 900 °C. Moreover, during the preparation of NG-SCC_f the remaining g-C_3N_4 sacrificial template

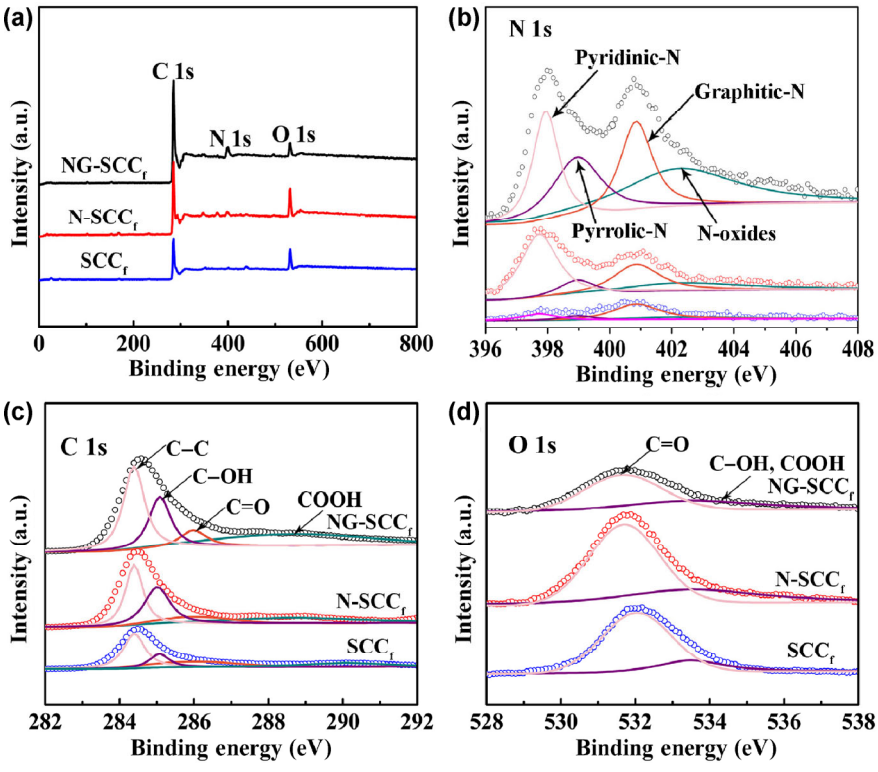

Figure 2 (a) XPS survey and (b)–(d) corresponding high-resolution N 1s, C 1s, and O 1s spectra of NG-SCC$_f$, N-SCC$_f$, and SCC$_f$.

Table 1 Chemical composition (at.%) and content of graphitic and pyridinic N (at.%) for NG-SCC$_f$, N-SCC$_f$, and SCC$_f$

Sample	C	O	N	Graphitic-N	Pyridinic-N
NG-SCC$_f$	87.96	4.85	7.19	1.89	1.69
N-SCC$_f$	84.80	11.49	3.71	0.93	1.65
SCC$_f$	82.46	15.46	2.08	1.10	0.36

serves as a nitrogen source for further graphene doping and reduces the associated nitrogen leaching above 600 ℃.

A detailed overview of the chemical states of N is shown in Fig. 2(b). The N 1s spectra of the three samples can be deconvoluted into signals due to pyridinic N (~398.0 eV), pyrrolic N (~399.0 eV), graphitic N (~400.9 eV), and N oxides (~402.2 eV) [38]. Pyridinic and graphitic nitrogens [39] are generally regarded as active sites beneficial for the ORR. The defect density can be efficiently enhanced after the *in situ* growth of graphene. We believe that NG-SCC$_f$ can provide more active sites and offer potential for the enhancement of electrocatalytic activity. Furthermore, proper hydrophilicity is essential to improve the ORR mass transport. Therefore, we also performed a detailed analysis of the chemical states of C and O in NG-SCC$_f$ (Figs. 2(c) and 2(d)). The results indicate the existence of C–OH and C=O functionalities, which can improve the hydrophilicity of the carbon plane and allow the electrolyte with dissolved O_2 to reach the catalytically active sites more easily [40].

The following mechanism for the formation of the *in situ* grown NG is proposed. During thermal treatment of the silk cocoon/melamine/g-C_3N_4 mixture, the silk cocoon acts as a precursor to SCC$_f$ and liberates plenty of carbonaceous gases. The carbon intermediates diffuse into the interlayer voids of g-C_3N_4 and are thermally transformed into graphene. When heated at low temperature (≤600 ℃), melamine polymerizes to supply more g-C_3N_4, and the evolved nitrogenous gases gradually dope SCC$_f$ and graphene. When heated to 900 ℃, g-C_3N_4 decomposes completely [20, 24]. The released nitrogenous intermediates function as nitrogen dopant precursors for both graphene and SCC$_f$, thus leading to the formation of NG. As a comparison, no graphene formed when the SCC$_f$/melamine/g-C_3N_4 mixture was pyrolyzed under the same condition,

mainly due to the fact that no carbon intermediates participated in the reaction.

XRD patterns (Fig. 3(a)) were recorded to characterize the degree of graphitization. All three samples exhibit two broad peaks at 2θ = 26° and 43°, attributed to the (002) and (100) facets of the graphitic material, respectively, indicating a low graphitization degree [41–43]. Furthermore, the corresponding Raman spectra (Fig. 3(b)) were also recorded. The D band near 1,360 cm^{-1} and G band close to 1,580 cm^{-1} are attributed to the disordered and ordered structures of the carbon material, respectively [44]. Generally, the band intensity ratio (I_D/I_G) is used to measure the amount of defects in the carbon structure [45]. NG-SCC_f shows a higher I_D/I_G value (1.01) than N-SCC_f (0.88), indicating a higher amount of disordered carbon and supposedly related to enhanced N content and *in situ* formed NG. Besides, thermal stability is a key factor for practical applications. TGA carried out in an atmosphere of N_2 demonstrates that NG-SCC_f has superior thermal stability (Fig. S1 in the Electronic Supplementary Material (ESM)).

Large S_{BET} and pore volume are highly desirable for the enhancement of ORR activity [46]. To analyze the pore structure of SCC_f and NG-SCC_f, N_2 adsorption–desorption experiments were carried out at 77 K (Fig. 4). SCC_f exhibits an isotherm of type IV, and its S_{BET} (Fig. 4(a)) was calculated to be 1,032.1 $m^2 \cdot g^{-1}$; the average pore diameter was estimated at 1.96 nm. At low p/p_0 values (p/p_0 < 0.1), SCC_f exhibited rapid adsorption increase attributed to the presence of micropores [47]. Therefore, SCC_f contains micro-, meso-, and macropores. The isotherm of NG-SCC_f (Fig. 4(b)) is of type III, with a hysteresis loop at medium and high pressure (p/p_0 = 0.4–1.0), attributable to the existence of meso- and macropores [48]. The corresponding S_{BET} was calculated to be 133.5 $m^2 \cdot g^{-1}$, and the average pore diameter was estimated at 8.15 nm, with a peak at 2.15 nm. Obviously, the formation of NG led to almost complete disappearance of the micropores. Since the fibrous frameworks formed by carbon nanoparticles are linked together, NG-SCC_f exhibits an interconnected meso-/macroporous structure, which can improve adsorption performance and generate

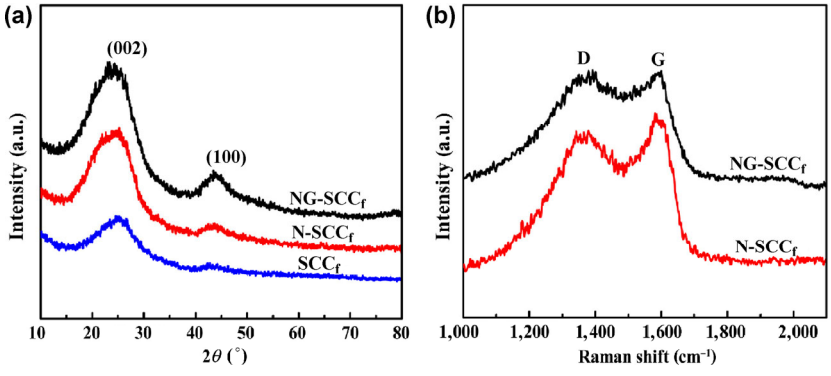

Figure 3 (a) XRD patterns of NG-SCC_f, N-SCC_f, and SCC_f; (b) Raman spectra of NG-SCC_f and N-SCC_f.

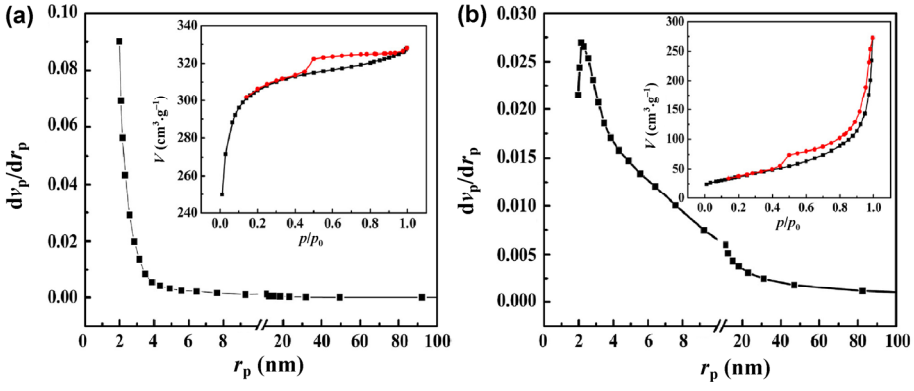

Figure 4 Nitrogen adsorption–desorption isotherms at 77 K (inset) and pore size distributions of (a) SCC_f and (b) NG-SCC_f.

multidimensional pathways to promote mass and electron transport [49]. Such interconnected porous web structure can also act as a perfect support for the ORR active sites.

To gain insight into the electrocatalytic ORR activities, CV and LSV tests were performed in O_2-saturated 0.1 M KOH solution. As shown in Fig. 5(a), NG-SCC$_f$ exhibits a more positive peak potential and a larger peak current (–0.234 V vs. SCE, 1.468 mA·cm^{-2}) than the other samples, signifying a better catalytic performance. Remarkably, the ORR onset potential of NG-SCC$_f$ (–0.148 V) is more positive than that of N-SCC$_f$ (–0.360 V), NG (–0.220 V), and the physical mixture of NG and N-SCC$_f$ (termed MIX) (–0.213 V), being slightly (by 0.1 V) inferior to that of Pt/C (Fig. 5(b)) at the same catalyst loading of 0.32 mg·cm^{-2}. In addition, NG-SCC$_f$ shows a comparable ORR activity to numerous other metal-free electrocatalysts, as shown in Table S1 (in the ESM). Moreover, NG-SCC$_f$ outperforms other catalysts, including N-SCC$_f$, NG, and MIX in terms of disk current density and half-wave potential, indicating its higher ORR electrocatalytic activity. Taken together, the strong synergistic coupling between the *in situ* grown NG and carbonized silk effectively improves the ORR activity.

The 4e$^-$ reduction pathway for ORR (Eq. (3)) is highly desired, while the less desirable 2e$^-$ reduction pathway (Eq. (4)) is not only inefficient, but also produces corrosive hydrogen peroxide. To understand the ORR mechanism and the main electrocatalytic process, we performed LSV measurements using different RDE rotation speeds. Figure 5(c) shows the RDE voltammograms of NG-SCC$_f$. The Koutecky–Levich (K–L) equation was used to analyze the kinetic parameters, and Fig. 5(d) shows the corresponding K–L plot with good linearity. The n value is calculated to be 3.51–3.93 at potentials between –0.50 and –0.70 V, suggesting that the ORR is dominated by the 4e$^-$ reduction pathway, similarly to Pt/C (Fig. 5(e)). Figure S2 in the ESM shows RDE voltammograms at various rotation speeds and the corresponding K–L plots of other samples. The n values are estimated to be 2.58–2.20 (N-SCC$_f$), 2.76–3.18 (NG), and 2.59–2.83 (MIX), implying that the ORR for these three samples occurs via the 2e$^-$ pathway. We also performed LSV analysis for SCC$_f$ (Fig. S3 in the ESM). Though SCC$_f$ has a high S_{BET}, its electrocatalytic activity is far lower than that of NG-SCC$_f$, indicating that N-doping and the *in situ* formed NG are more important than the surface area for enhancing ORR activity. Obviously, NG-SCC$_f$ has a higher active site density than SCC$_f$. Figure 5(f) is a schematic illustration of the 3D

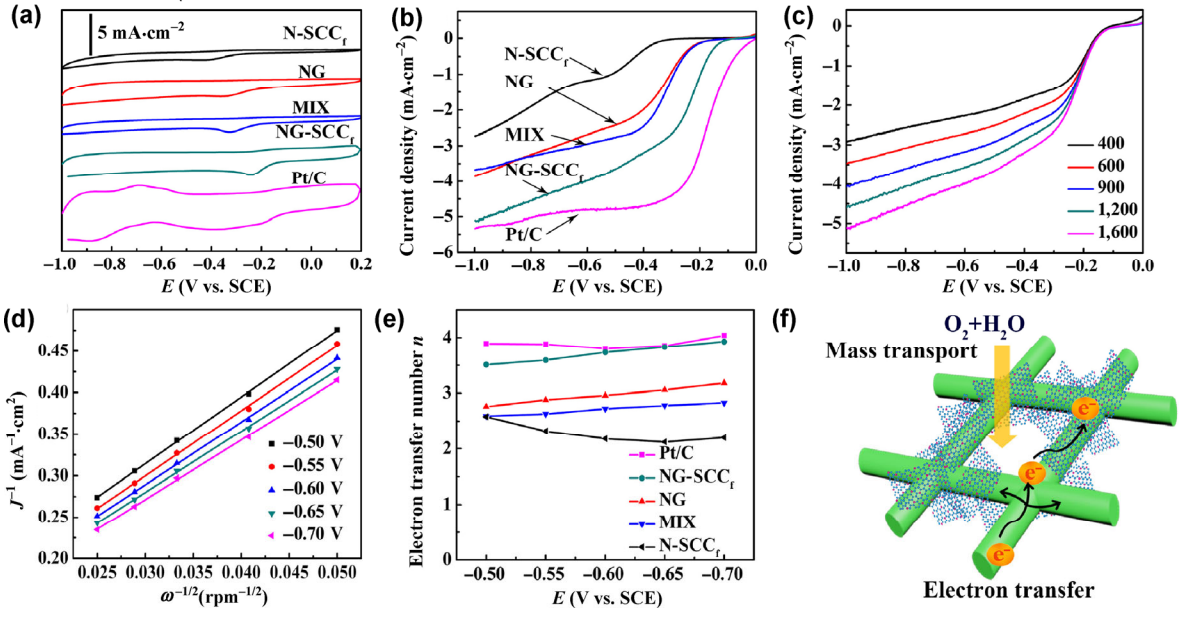

Figure 5 (a) CV and (b) LSV curves of N-SCC$_f$, NG, MIX, NG-SCC$_f$, and Pt/C at 1,600 rpm; (c) LSV curves at different rotation speeds, and (d) the corresponding K–L plots of NG-SCC$_f$; (e) electron transfer numbers of different samples; (f) schematic illustration of the 3D interconnected web structure of NG-SCC$_f$, facilitating electron transfer and mass transport.

interconnected web structure of NG-SCC$_f$. The interconnected SCC$_f$ with *in situ* grown NG provides more active sites and enables efficient electron transport through the whole framework. The large voids between interconnected fibers and the meso-/macropores ensure smooth mass transfer. The two aspects remarkably improve ORR diffusion kinetics.

$$O_2 + H_2O + 4e^- \rightarrow 4OH^- \quad (3)$$

$$O_2 + H_2O + 2e^- \rightarrow HO_2^- + OH^- \quad (4)$$

To validate the stability and methanol tolerance of NG-SCC$_f$, CV measurements were performed for up to 2,000 cycles in O_2-saturated 0.1 M KOH and in O_2-saturated 0.1 M KOH with 3 M methanol (Fig. 6). The original cathodic ORR peak potential and current do not exhibit distinct changes, highlighting excellent electrocatalytic stability in the ORR process (Fig. 6(a)). However, the Pt/C catalyst is less stable (Fig. 6(b)). As known for direct methanol FCs, methanol in the anode region may pass through the proton exchange membrane and get oxidized at the cathode, significantly deteriorating the cell performance [50, 51]. Thus, ORR catalysts should also exhibit satisfactory methanol tolerance. In this study, 3 M methanol was added to the 0.1 M KOH aqueous electrolyte. It is worth noting that the original cathodic ORR peak potential and current of NG-SCC$_f$ remains almost unchanged (Fig. 6(a)), whereas the CV curve of Pt/C is greatly affected by methanol addition (Fig. 6(b)). Therefore, NG-SCC$_f$ shows stability and methanol tolerance superior to those of Pt/C in alkaline media, appearing to be an alternative cathode catalyst for use in direct methanol alkaline FCs.

Based on the aforementioned results, the superior ORR performance of NG-SCC$_f$ can be mainly ascribed to four factors: 1) The meso- and macropores obtained as a result of the thermal treatment of silk cocoon can reduce diffusion resistance and ensure rapid mass transport; 2) the *in situ* formed NG is in intimate contact with cocoon-derived carbon fibers and forms favorable nitrogen species, providing effective active sites for ORR; 3) the interconnected 3D web structure of SCC$_f$ and the tough contact between NG and SCC$_f$ promote rapid electron transfer; 4) the proper hydrophilicity makes it easier for the electrolyte with dissolved O_2 to get to the catalytically active sites. The synergistic combination of the above advantages dramatically improves the electrocatalytic activity.

To show that our catalysts can also work well in other reactions, the photocatalytic performance of NG-SCC$_f$ was investigated. As known, photolytic water splitting is promising if low-cost semiconductors with scalable preparation routes are used [52–55]. Recently, growing demands for metal-free photocatalysts based on earth-abundant elements (e.g., g-C_3N_4) have attracted much attention [56–59]. As reported, C-N structures can be utilized to create semiconducting materials for photocatalytic applications [14]. Meanwhile, graphene shows the ability to effectively hinder charge recombination [60]. Inspired by these advances, the simply prepared, low-cost, and non-toxic NG-SCC$_f$ is expected to have superior photocatalytic activity. Thus, photocatalytic H_2 production under simulated solar light was investigated.

As shown in Fig. 7(a), SCC$_f$ (20 mg) shows an H_2

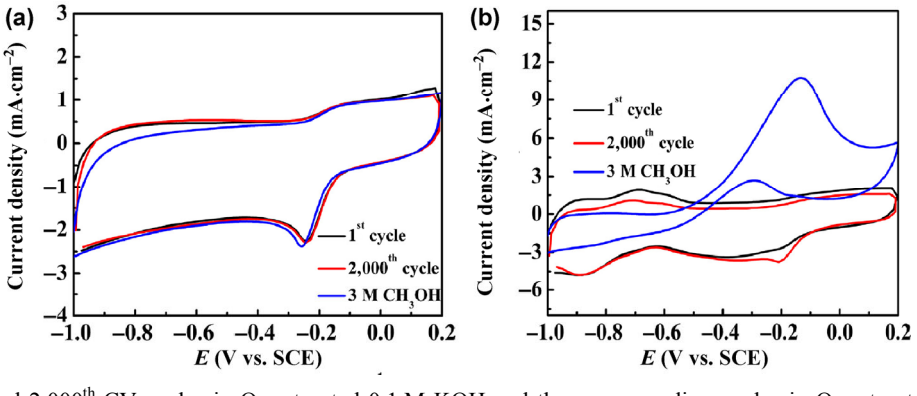

Figure 6 The 1st and 2,000th CV cycles in O_2-saturated 0.1 M KOH and the corresponding cycles in O_2-saturated 0.1 M KOH with 3 M methanol for (a) NG-SCC$_f$ and (b) Pt/C. Scan rate = 100 mV·s^{-1}.

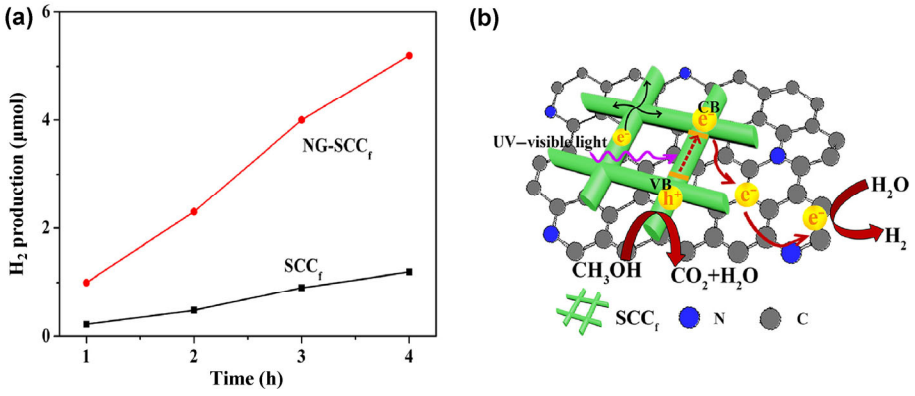

Figure 7 (a) Comparison of the time-dependent photocatalytic activities of SCC_f and NG-SCC_f (20 mg) for H_2 production and (b) a plausible schematic explanation of the enhanced photocatalytic H_2 production activity.

production rate of 0.30 μmol·h^{-1} (15 μmol·h^{-1}·g^{-1}), possibly resulting from a small amount of C-N structure derived from silk cocoon and a high S_{BET}. Excitingly, in absence of Pt as a co-catalyst, the metal-free NG-SCC_f (20 mg) shows an H_2 production rate of 1.32 μmol·h^{-1} (66.0 μmol·h^{-1}·g^{-1}), 4.4-fold higher than that of SCC_f. Considering that the S_{BET} of NG-SCC_f is much lower than that of SCC_f, S_{BET} cannot be the main factor influencing photocatalytic H_2 production. The dominant cause can be attributed to the higher nitrogen content, superior electron conductivity, and good hydrophilicity of NG-SCC_f. To elucidate the enhanced photocatalytic H_2 production activity, a control experiment was performed using NG prepared from GO and melamine, where no H_2 production was detected. Hence, a plausible mechanism for the production of H_2 was proposed, shown in Fig. 7(b). The interconnected SCC_f fibers provide multiple paths enhancing electron transport, and the *in situ* formed NG allows rapid transport of charge carriers as well as effective separation of electron–hole pairs [61], thus accelerating the reduction process to generate H_2. Hence, the NG-SCC_f material is an appealing candidate for metal-free photocatalytic materials. Further investigations are currently under way.

4 Conclusions

In summary, we have successfully prepared 3D interconnected carbon fibers with *in situ* grown NG by a one-step thermal treatment. This work successfully combines the advantages of NG, having numerous active sites, with those of the hierarchically interconnected porous SCC_f, exhibiting high electron conductivity and abundant meso- /macropores, etc. Due to its superior ORR activity, excellent stability, good methanol tolerance, and a low-cost scalable synthesis, NG-SCC_f presents a potential alternative to Pt/C as an ORR catalyst. In addition, it also exhibits good solar photocatalytic H_2 production activity, mainly due to its interconnected structure, hierarchical pores, and a high nitrogen content of the *in situ* formed NG. A bifunctional catalyst for both photocatalytic H_2 production and ORR could be very promising for sustainable development. NG-SCC_f can also act as a support for the loading of photo-/electrocatalytic species to achieve enhanced properties. Furthermore, this work might provide a simple way to prepare metal-free catalysts with well-tailored architecture and composition for applications in energy- and environment-related fields.

Acknowledgements

The work was financially supported by National Natural Science Foundation of China (Nos. 51203182 and 51173202), Foundation for the Author of Excellent Doctoral Dissertation of Hunan Province (No. YB2014B004), Aeronautical Science Foundation of China (No. 20143188004), Key Laboratory of Advanced Textile Materials and Manufacturing Technology (Zhejiang Sci-Tech University), Ministry of Education

(No. 2015001), Key Laboratory of Lightweight and Reliability Technology for Engineering Vehicle, College of Hunan Province (No. 2016kfjj01), Research Project of NUDT. We thank Tengyuan Wang for help in ORR experiment and helpful discussions.

Electronic Supplementary Material: Supplementary material (TGA curves, LSVs, K–L plots, and ORR activity of different non-metal catalysts) is available in the online version of this article at http://dx.doi.org/10.1007/s12274-016-1136-4.

References

[1] Liu, Y. M.; Chen, S.; Quan, X.; Yu, H. T.; Zhao, H. M.; Zhang, Y. B.; Chen, G. H. Boron and nitrogen codoped nanodiamond as an efficient metal-free catalyst for oxygen reduction reaction. *J. Phys. Chem. C* **2013**, *117*, 14992–14998.

[2] Gong, K. P.; Du, F.; Xia, Z. H.; Durstock, M.; Dai, L. M. Nitrogen-doped carbon nanotube arrays with high electrocatalytic activity for oxygen reduction. *Science* **2009**, *323*, 760–764.

[3] Chu, S.; Majumdar, A. Opportunities and challenges for a sustainable energy future. *Nature* **2012**, *488*, 294–303.

[4] Kim, J. Y.; Oh, T. K.; Shin, Y.; Bonnett, J.; Weil, K. S. A novel non-platinum group electrocatalyst for PEM fuel cell application. *Int. J. Hydrogen Energ.* **2011**, *36*, 4557–4564.

[5] Huang, D. K.; Zhang, B. Y.; Li, S. H.; Wang, M. K.; Shen, Y. Mn_3O_4/carbon nanotube nanocomposites as electrocatalysts for the oxygen reduction reaction in alkaline solution. *ChemElectroChem* **2014**, *1*, 1531–1536.

[6] Gao, X. P.; Yang, H. X. Multi-electron reaction materials for high energy density batteries. *Energy Environ. Sci.* **2010**, *3*, 174–189.

[7] Lin, Z. Y.; Waller, G. H.; Liu, Y.; Liu, M. L.; Wong, C. P. Simple preparation of nanoporous few-layer nitrogen-doped graphene for use as an efficient electrocatalyst for oxygen reduction and oxygen evolution reactions. *Carbon* **2013**, *53*, 130–136.

[8] Wang, S. Y.; Zhang, L. P.; Xia, Z. H.; Roy, A.; Chang, D. W.; Baek, J. B.; Dai, L. M. BCN graphene as efficient metal-free electrocatalyst for the oxygen reduction reaction. *Angew. Chem., Int. Ed.* **2012**, *51*, 4209–4212.

[9] Zhang, Y.; Zhuang, X. D.; Su, Y. Z.; Zhang, F.; Feng, X. L. Polyaniline nanosheet derived B/N co-doped carbon nanosheets as efficient metal-free catalysts for oxygen reduction reaction. *J. Mater. Chem. A* **2014**, *2*, 7742–7746.

[10] Yang, S. B.; Feng, X. L.; Wang, X. C.; Müllen, K. Graphene-based carbon nitride nanosheets as efficient metal-free electrocatalysts for oxygen reduction reactions. *Angew. Chem., Int. Ed.* **2011**, *50*, 5339–5343.

[11] Wang, S. Y.; Iyyamperumal, E.; Roy, A.; Xue, Y. H.; Yu, D. S.; Dai, L. M. Vertically aligned BCN nanotubes as efficient metal-free electrocatalysts for the oxygen reduction reaction: A synergetic effect by co-doping with boron and nitrogen. *Angew. Chem., Int. Ed.* **2011**, *50*, 11756–11760.

[12] Liu, D.; Zhang, X. P.; Sun, Z. C.; You, T. Y. Free-standing nitrogen-doped carbon nanofiber films as highly efficient electrocatalysts for oxygen reduction. *Nanoscale* **2013**, *5*, 9528–9531.

[13] Dai, L. M.; Xue, Y. H.; Qu, L. T.; Choi, H. J.; Baek, J. B. Metal-free catalysts for oxygen reduction reaction. *Chem. Rev.* **2015**, *115*, 4823–4892.

[14] Wood, K. N.; O'Hayre, R.; Pylypenko, S. Recent progress on nitrogen/carbon structures designed for use in energy and sustainability applications. *Energy Environ. Sci.* **2014**, *7*, 1212–1249.

[15] Zhong, R. S.; Qin, Y. H.; Niu, D. F.; Tian, J. W.; Zhang, X. S.; Zhou, X. G.; Yuan, W. K. Effect of carbon nanofiber surface functional groups on oxygen reduction in alkaline solution. *J. Power Sources* **2013**, *225*, 192–199.

[16] Shi, Q.; Lei, Y. P.; Wang, Y. D.; Wang, H. P.; Jiang, L. H.; Yuan, H. L.; Fang, D.; Wang, B.; Wu, N.; Gou, Y. Z. B, N-codoped 3D micro-/mesoporous carbon nanofibers web as efficient metal-free catalysts for oxygen reduction. *Curr. Appl. Phys.* **2015**, *15*, 1606–1614.

[17] Wang, X. R.; Li, X. L.; Zhang, L.; Yoon, Y.; Weber, P. K.; Wang, H. L.; Guo, J.; Dai, H. J. N-doping of graphene through electrothermal reactions with ammonia. *Science* **2009**, *324*, 768–771.

[18] Li, X. H.; Antonietti, M. Polycondensation of boron- and nitrogen-codoped holey graphene monoliths from molecules: Carbocatalysts for selective oxidation. *Angew. Chem., Int. Ed.* **2013**, *52*, 4572–4576.

[19] Li, Y. G.; Zhou, W.; Wang, H. L.; Xie, L. M; Liang, Y. Y.; Wei, F.; Idrobo, J. C.; Pennycook, S. J.; Dai, H. J. An oxygen reduction electrocatalyst based on carbon nanotube-graphene complexes. *Nat. Nanotechnol.* **2012**, *7*, 394–400.

[20] Liang, J.; Du, X.; Gibson, C.; Du, X. W.; Qiao, S. Z. N-doped graphene natively grown on hierarchical ordered porous carbon for enhanced oxygen reduction. *Adv. Mater.* **2013**, *25*, 6226–6231.

[21] Raymundo-Piñero, E.; Cadek, M.; Béguin, F. Tuning carbon materials for supercapacitors by direct pyrolysis of seaweeds. *Adv. Funct. Mater.* **2009**, *19*, 1032–1039.

[22] Guo, C. Z.; Liao, W. L.; Li, Z. B.; Chen, C. G. Exploration of the catalytically active site structures of animal biomass-modified on cheap carbon nanospheres for oxygen reduction reaction with high activity, stability and methanol-tolerant performance in alkaline medium. *Carbon* **2015**, *85*, 279–288.

[23] Ling, Z.; Wang, Z. Y.; Zhang, M. D.; Yu, C.; Wang, G.; Dong, Y. F.; Liu, S. H.; Wang, Y. W.; Qiu, J. S. Sustainable synthesis: Sustainable synthesis and assembly of biomass-derived B/N co-doped carbon nanosheets with ultrahigh aspect ratio for high-performance supercapacitors. *Adv. Funct. Mater*. **2016**, *26*, 111–119.

[24] Ye, T. N.; Lv, L. B.; Li, X. H.; Xu, M.; Chen, J. S. Strongly veined carbon nanoleaves as a highly efficient metal-free electrocatalyst. *Angew. Chem., Int. Ed*. **2014**, *53*, 6905–6909.

[25] Huang, Y. Y.; Wu, P.; Wang, Y. B.; Wang, W. J.; Yuan, D. Q.; Yao, J. N. Ideal N-doped carbon nanoarchitectures evolved from fibrils for highly efficient oxygen reduction. *J. Mater. Chem. A* **2014**, *2*, 19765–19770.

[26] Gao, S. Y.; Geng, K. R.; Liu, H. Y.; Wei, X. J.; Zhang, M.; Wang, P.; Wang, J. J. Transforming organic-rich amaranthus waste into nitrogen-doped carbon with superior performance of the oxygen reduction reaction. *Energy Environ. Sci*. **2015**, *8*, 221–229.

[27] Guo, Z. Y.; Xiao, Z.; Ren, G. Y.; Xiao, G. Z.; Zhu, Y.; Dai, L. M.; Jiang, L. Natural tea-leaf-derived, ternary-doped 3D porous carbon as a high-performance electrocatalyst for the oxygen reduction reaction. *Nano Res*. **2016**, *9*, 1244–1255.

[28] Chaudhari, K. N.; Song, M. Y.; Yu, J. S. Transforming hair into heteroatom-doped carbon with high surface area. *Small* **2014**, *10*, 2625–2636.

[29] Peng, S. J.; Jin, G. R.; Li, L. L.; Li, K.; Srinivasan, M.; Ramakrishna, S.; Chen, J. Multi-functional electrospun nanofibres for advances in tissue regeneration, energy conversion & storage, and water treatment. *Chem. Soc. Rev*. **2016**, *45*, 1225–1241.

[30] Park, H. W.; Lee, D. U.; Zamani, P.; Seo., M. H.; Nazar, L. F.; Chen, Z. W. Electrospun porous nanorod perovskite oxide/nitrogen-doped graphene composite as a bi-functional catalyst for metal air batteries. *Nano Energy* **2014**, *10*, 192–200.

[31] Wang, B.; Wang, Y. D.; Lei, Y. P.; Xie, S.; Wu, N.; Gou, Y. Z.; Han, C.; Shi, Q.; Fang, D. Vertical SnO_2 nanosheet@SiC nanofibers with hierarchical architecture for high-performance gas sensors. *J. Mater. Chem. C* **2016**, *4*, 295–304.

[32] Liang, Y. R.; Wu, D. C.; Fu, R. W. Carbon microfibers with hierarchical porous structure from electrospun fiber-like natural biopolymer. *Sci. Rep*. **2013**, *3*, 1119.

[33] Wu, N.; Wang, Y. D.; Lei, Y. P.; Wang, B.; Han, C.; Gou, Y. Z.; Shi, Q.; Fang, D. Electrospun interconnected Fe-N/C nanofiber networks as efficient electrocatalysts for oxygen reduction reaction in acidic media. *Sci. Rep*. **2015**, *5*, 17396.

[34] Shi, Q.; Wang, Y. D.; Wang, Z. M.; Lei, Y. P.; Wang, B.; Wu, N.; Han, C.; Xie, S.; Gou, Y. Z. Three-dimensional (3D) interconnected networks fabricated via *in-situ* growth of N-doped graphene/carbon nanotubes on Co-containing carbon nanofibers for enhanced oxygen reduction. *Nano Res*. **2016**, *9*, 317–328.

[35] Shi, Q.; Lei, Y. P.; Wang, Y. D.; Wang, Z. M. *In-situ* preparation and electrocatalytic oxygen reduction performance of N-doped graphene@CNF. *J. Inorg. Mater*. **2016**, *31*, 351–357.

[36] Marcano, D. C.; Kosynkin, D. V.; Berlin, J. M.; Sinitskii, A.; Sun, Z. Z.; Slesarev, A.; Alemany, L. B.; Lu, W.; Tour, J. M. Improved synthesis of graphene oxide. *ACS Nano* **2010**, *4*, 4806–4814.

[37] Li, L. J.; Manthiram, A. O-and N-doped carbon nanowebs as metal-free catalysts for hybrid Li-air batteries. *Adv. Energy Mater*. **2014**, *4*, 1301795.

[38] Ma, R. G.; Xia, B. Y.; Zhou, Y.; Li, P. X.; Chen, Y. F.; Liu, Q.; Wang, J. C. Ionic liquid-assisted synthesis of dual-doped graphene as efficient electrocatalysts for oxygen reduction. *Carbon* **2016**, *102*, 58–65.

[39] Liang, J.; Jiao, Y.; Jaroniec, M.; Qiao, S. Z. Sulfur and nitrogen dual-doped mesoporous graphene electrocatalyst for oxygen reduction with synergistically enhanced performance. *Angew. Chem., Int. Ed*. **2012**, *51*, 11496–11500.

[40] Lee, J. S.; Park, G. S.; Kim, S. T.; Liu, M. L.; Cho, J. A highly efficient electrocatalyst for the oxygen reduction reaction: N-doped ketjenblack incorporated into Fe/Fe_3C-functionalized melamine foam. *Angew. Chem., Int. Ed*. **2013**, *125*, 1060–1064.

[41] Kang, Y.; Chu, Z. Y.; Zhang, D. J.; Li, G. Y.; Jiang, Z. H.; Cheng, H. F.; Li, X. D. Incorporate boron and nitrogen into graphene to make BCN hybrid nanosheets with enhanced microwave absorbing properties. *Carbon* **2013**, *61*, 200–208.

[42] Wang, Y. D.; Han, C.; Zheng, D. C.; Lei, Y. P. Large-scale, flexible and high-temperature resistant ZrO_2/SiC ultrafine fibers with a radial gradient composition. *J. Mater. Chem. A* **2014**, *2*, 9607–9612.

[43] Raidongia, K.; Nag, A.; Hembram, K. P. S. S.; Waghmare, U. V.; Datta, R.; Rao, C. N. R. BCN: A graphene analogue with remarkable adsorptive properties. *Chem.—Eur. J*. **2010**, *16*, 149–157.

[44] Ma, Y.; Wang, S.; Chen, Z. H. *In situ* growth of a carbon interphase between carbon fibres and a polycarbosilane-derived silicon carbide matrix. *Carbon* **2011**, *49*, 2869–2872.

[45] Zhao, Y.; Hu, C. G.; Hu, Y.; Cheng, H. H.; Shi, G. Q.; Qu, L. T. A versatile, ultralight, nitrogen-doped graphene framework. *Angew. Chem., Int. Ed*. **2012**, *51*, 11371–11375.

[46] Xu, J. X.; Zhao, Y.; Shen, C.; Guan, L. H. Sulfur- and nitrogen-doped, ferrocene-derived mesoporous carbons with efficient electrochemical reduction of oxygen. *ACS Appl. Mater. Interface* **2013**, *5*, 12594–12601.

[47] Chen, L. H.; Li, X. Y.; Tian, G.; Li, Y.; Tan, H. Y.; van Tendeloo, G.; Zhu, G. S.; Qiu, S. L.; Yang, X. Y.; Su, B. L. Multimodal zeolite-beta-based catalysts with a hierarchical, three-level pore structure. *ChemSusChem* **2011**, *4*, 1452–1456.

[48] Liang, J.; Zhou, R. F.; Chen, X. M.; Tang, Y. H.; Qiao, S. Z. Fe-N decorated hybrids of CNTs grown on hierarchically porous carbon for high-performance oxygen reduction. *Adv. Mater*. **2014**, *26*, 6074–6079.

[49] Chen, R. X.; Yu, J. G.; Xiao, W. Hierarchically porous MnO_2 microspheres with enhanced adsorption performance. *J. Mater. Chem. A* **2013**, *1*, 11682–11690.

[50] Liang, J.; Zheng, Y.; Chen, J.; Liu, J.; Hulicova-Jurcakova, D.; Jaroniec, M.; Qiao, S. Z. Facile oxygen reduction on a three-dimensionally ordered macroporous graphitic C_3N_4/carbon composite electrocatalyst. *Angew. Chem., Int. Ed*. **2012**, *51*, 3892–3896.

[51] Qu, L. T.; Liu, Y.; Baek, J. B.; Dai, L. M. Nitrogen-doped graphene as efficient metal-free electrocatalyst for oxygen reduction in fuel cells. *ACS Nano* **2010**, *4*, 1321–1326.

[52] Liu, Y. X.; Zhang, B. S.; Luo, L. F.; Chen, X. Y.; Wang, Z. L.; Wu, E. L.; Su, D. S.; Huang, W. X. TiO_2/Cu_2O core/ultrathin shell nanorods as efficient and stable photocatalysts for water reduction. *Angew. Chem., Int. Ed*. **2015**, *54*, 15260–15265.

[53] Zhou, Y. X.; Lei, Y. P.; Wang, D. S.; Chen, C.; Peng, Q.; Li, Y. D. Ultra-thin Cu_2S nanosheets: Effective cocatalysts for photocatalytic hydrogen production. *Chem. Commun*. **2015**, *51*, 13305–13308.

[54] Han, Q.; Zhao, F.; Hu, C. G.; Lv, L. X.; Zhang, Z. P.; Chen, N.; Qu, L. T. Facile production of ultrathin graphitic carbon nitride nanoplatelets for efficient visible-light water splitting. *Nano Res*. **2015**, *8*, 1718–1728.

[55] Hao, R.; Jiang, B. J.; Li, M. X.; Xie, Y.; Fu, H. G. Fabrication of mixed-crystalline-phase spindle-like TiO_2 for enhanced photocatalytic hydrogen production. *Sci. China Mater*. **2015**, *58*, 363–369.

[56] Wang, X. C.; Maeda, K.; Thomas, A.; Takanabe, K.; Xin, G.; Carlsson, J. M.; Domen, K.; Antonietti, M. A metal-free polymeric photocatalyst for hydrogen production from water under visible light. *Nat. Mater*. **2009**, *8*, 76–80.

[57] Cao, S. W.; Low, J. X.; Yu, J. G.; Jaroniec, M. Polymeric photocatalysts based on graphitic carbon nitride. *Adv. Mater*. **2015**, *27*, 2150–2176.

[58] Han, C.; Wang, Y. D.; Lei, Y. P.; Wang, B.; Wu, N.; Shi, Q.; Li, Q. *In situ* synthesis of graphitic-C_3N_4 nanosheet hybridized N-doped TiO_2 nanofibers for efficient photocatalytic H_2 production and degradation. *Nano Res*. **2015**, *8*, 1199–1209.

[59] Li, X.; Wen, J. Q.; Low, J.; Fang, Y. P.; Yu, J. G. Design and fabrication of semiconductor photocatalyst for photocatalytic reduction of CO_2 to solar fuel. *Sci. China Mater*. **2014**, *57*, 70–100.

[60] Lightcap, I. V.; Kosel, T. H.; Kamat, P. V. Anchoring semiconductor and metal nanoparticles on a two-dimensional catalyst mat. storing and shuttling electrons with reduced graphene oxide. *Nano Lett*. **2010**, *10*, 577–583.

[61] Tan, L. L.; Chai, S. P.; Mohamed, A. R. Synthesis and applications of graphene-based TiO_2 photocatalysts. *ChemSusChem* **2012**, *5*, 1868–1882.